Role of diffused Co atoms in improving effective exchange coupling in Sm-Co/Fe spring magnets

Y. Choi,[1,2] J. S. Jiang,[1] Y. Ding,[3] R. A. Rosenberg,[4] J. E. Pearson,[1] S. D. Bader,[1] A. Zambano,[5] M. Murakami,[5] I. Takeuchi,[5] Z. L. Wang,[3] and J. P. Liu[2]

[1]*Materials Science Division, Argonne National Laboratory, Argonne, Illinois 60439, USA*
[2]*Department of Physics, University of Texas at Arlington, Arlington, Texas 76019, USA*
[3]*School of Materials Science and Engineering, Georgia Institute of Technology, Atlanta, Georgia 30332, USA*
[4]*Advanced Photon Source, Argonne National Laboratory, Argonne, Illinois 60439, USA*
[5]*Department of Materials Science and Engineering, University of Maryland, College Park, Maryland 20742, USA*

In Sm-Co/Fe exchange-spring magnet films, the magnetization reversal processes of constituent elements and layers were studied with an emphasis on the role of diffused Co atoms. Enhanced coupling effectiveness was observed in a film with a graded interface where significant Co diffusion into the Fe layer was observed by means of electron microscopy. Comprehensive insight into the magnetization reversal processes was obtained by combining micromagnetic simulation with element- and depth-resolved x-ray resonant magnetic scattering. The approach unambiguously identifies distinctive composition profiles across the graded interface and provides the magnetization behavior of the diffused Co.

I. INTRODUCTION

Exchange-spring permanent magnets have the potential to achieve very high energy product values by taking advantage of the high magnetic anisotropy of a magnetically hard phase and the high saturation moment of a magnetically soft phase.[1,2] Sm-Co/Fe bilayer films provide a structure for systemically investigating the magnetization processes in nanocomposite spring magnets. In layered structures, the magnetic anisotropy configuration and structural parameters can be readily controlled, thus making them an ideal model system for studying the fundamental properties of exchange-spring magnets.[3–6] In a Sm-Co/Fe magnet, the maximum energy product achievable is limited by a low nucleation field of the soft Fe phase. The effectiveness of the interphase exchange coupling at the Sm-Co/Fe interface plays a crucial role in the overall magnetic properties, since the exchange coupling is strongly related to the Fe nucleation field. Thermal annealing is known to enhance the nucleation field, suggesting the importance of a graded interface between the two phases in improving the energy product.[7]

In this paper, we report a study of the relationship of magnetic and interfacial modifications induced by different growth temperatures for the Fe layer in Sm-Co/Fe bilayers. A higher Fe growth temperature enhances intermixing and diffusion at the Sm-Co/Fe interface. The magnetization reversal process was probed via element-specific hysteresis loops based on x-ray resonant magnetic scattering (XRMS).[8,9] By resolving the magnetic response of each element, XRMS provides insight into how magnetic exchange interactions and microstructural changes influence the aggregate response of the overall system. To analyze the XRMS result, micromagnetic magnetization reversal curves along with electric field intensity profiles were calculated on the same film structure that was modeled with diffused concentration profiles. The experimental and computational results show good agreement, providing a unique insight into the magnetization reversal process and the role of Co diffusion across a graded interface.

II. EXPERIMENTAL DETAILS

Two Sm-Co/Fe exchange-spring bilayer samples were fabricated on MgO(110) substrates using magnetron sputtering.[3,7] The films have the sequence MgO/Cr(20 nm)/Sm-Co(20 nm)/Fe(20 nm)/Cr(5 nm). A buffer layer of 20 nm of Cr(211) and then a nominally Sm_2Co_7 layer were grown at 400 °C. On top of the Sm_2Co_7 layer, an Fe layer was grown at 100 or 400 °C (labeled *T*100 and *T*400, respectively, henceforth), and then a Cr capping layer was grown at 100 °C for each sample.

In order to study the correlation between the structural and magnetic modifications, magnetic characterization was performed at room temperature using vibrating sample magnetometry (VSM) and structural characterization was done with cross-sectional transmission electron microscopy (TEM). While VSM measures the aggregate magnetic response from the samples, a more complete description of the magnetization behavior can be obtained from magnetometry that utilizes element-specific XRMS. XRMS takes advantage of the enhanced magnetic sensitivity of a particular element when the incoming x-ray energy is tuned to an absorption edge of the element. In XRMS, the difference in resonant scattered intensities between left- and right-circularly-polarized x rays provides the magnetization of the element. This asymmetry is the measured XRMS signal. We measured XRMS signals at the Fe L_3, Co L_3, and Sm M_4 absorption edges in specular reflectivity mode. The XRMS measurements were performed at beamline 4ID-C of the Advanced Photon Source at Argonne National Laboratory.[10] The magnetic field was applied parallel or antiparallel to the incoming x-ray propagation direction; thus we probed the laterally averaged magnetization component along the field direction. Element-specific magnetization curves were obtained by collecting the normalized dichroic signals at $T=200$ K as a function of external magnetic field H. The applied field direction was along the easy axis of each sample. Each sample was magnetically saturated at $H=2$ T before each curve and at $H=-2$ T afterward.

Since the x-ray incident angle was low for the XRMS measurements ($\approx 10°$),[11] the signals are dominated by the upper layers due to the attenuation effect. This is important in the interpretation of the XRMS data. To account for the low-angle attenuation effect, we calculated the electric field intensity profiles inside the film layers using Parratt's recursive formula.[12,13] In these calculations, we used experimentally obtained x-ray optical constants for resonant Sm, Co, and Fe atoms[14,15] and tabulated nonresonant values.[16] For each sample, the electric field intensity profiles were calculated based on a model film structure that was approximated by one set of Sm, Co, and Fe concentration profiles.

III. MODELING DETAILS

In order to gain insight into the relationship between the interface characteristics and magnetic properties, magnetization curves for the Sm-Co/Fe bilayers were modeled using the LLG micromagnetics simulator.[17] The micromagnetic simulations were based on the same model film structures that were used in the electric field calculations. The bilayer Sm-Co (20 nm)/Fe (20 nm) was divided into a one dimensional chain of 40 simulation cells with 1 nm thickness. This modeling assumes lateral uniformity and coherent magnetization rotation. For the bilayer simulation, the same material parameters used in Ref. 3 were used except for the intermixed region. Across the Sm-Co/Fe interface, the material parameters (uniaxial anisotropy K_1, saturation magnetization M_s, exchange constant A) were gradually changed for the given compositions. Intermixing between Sm-Co and Fe likely forms a pseudobinary Sm-(Co,Fe) compound. It has been found that the addition of Fe in a $Sm_2(Co_{1-x}Fe_x)_{17}$ alloy phase increases the saturation magnetization while continuously changing the Curie temperature.[18–20] However, because of the lack of detailed data available for the magnetic parameters of $Sm_2(Co_{1-x}Fe_x)_{17}$, we assumed a simple dilution effect for these parameters.

IV. RESULTS AND DISCUSSION

Room temperature demagnetization curves of the two samples using VSM are shown in Fig. 1. In comparison with the $T100$ sample, the $T400$ sample exhibits an increased nucleation field and a decreased irreversible switching field. A similar trend has been observed on Sm-Co/Fe (Ref. 7) and on CoPt/Co (Refs. 4 and 5) films after annealing, and the observed changes in the nucleation and irreversible switching fields have been attributed to an enhanced effectiveness of exchange coupling.

The $T100$ and $T400$ samples are expected to have different interfacial morphologies due to the different growth conditions, and cross-sectional TEM images as shown in Fig. 2 confirm this. At the Sm-Co/Fe interfaces, the $T400$ sample shows a smoother interface morphology with less structural roughness. To check the elemental composition and interface diffusion, we measured energy-dispersive spectroscopy (EDS) data in scanning TEM mode. In Fig. 3, the intensity profiles of each element are plotted as a function of position. The profiles of the $T400$ sample are slightly broader overall
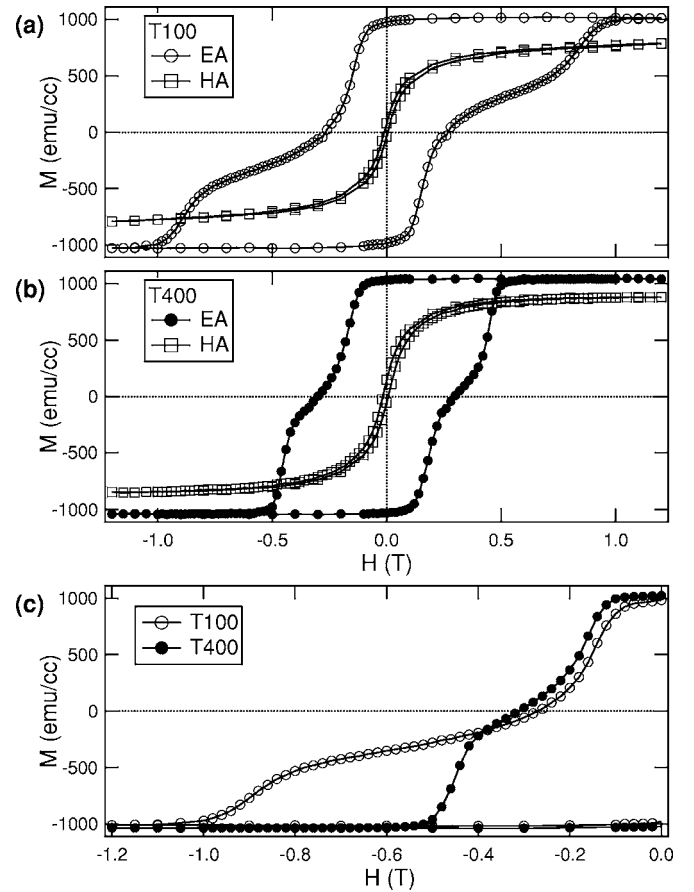

FIG. 1. In-plane easy and hard axis VMS measurements at room temperature for the $T100$ and $T400$ samples are shown in (a) and (b). (c) Easy axis demagnetization curves.

due to interdiffusion, and Co diffusion into the Fe layer is more pronounced [Fig. 3(b)], indicating composition modifications in the Fe and Sm-Co layers near the interface. Based on the EDS results, intermixing effects are expected to be present in both samples. However, the higher Fe growth temperature of the $T400$ sample leads to a morphologically smoother and more intermixed interface. The increased intermixing in the $T400$ sample gives rise to more gradual changes in the anisotropy and exchange constant profiles, leading to an improved coupling effectiveness, as evidenced by the increased nucleation field and decreased irreversible switching field in Fig. 1(c).

As described above, the aggregate magnetic responses are different between the two samples due to their different interfacial morphologies. Using the element-specific XRMS magnetometry, we measured Fe-, Co-, and Sm-specific magnetization curves at 200 K from the two samples as shown in Fig. 4. At the same temperature, superconducting quantum interference device (SQUID) measurements [Fig. 4(d)], sensitive to the overall magnetic response, show that the nucleation field of the $T400$ sample is higher than that of the $T100$ sample. The Fe magnetization curves in Fig. 4(a) show a similar trend of a higher nucleation field for the $T400$ sample. The Sm curves in Fig. 4(c) also show similar switching fields as the SQUID results. A significant difference between the two samples is noticeable in the Co curves [Fig.
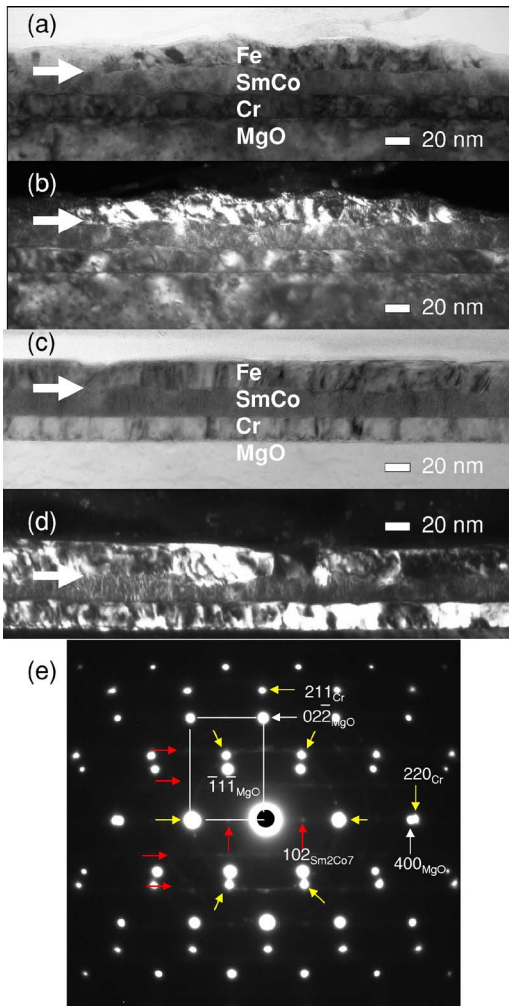
FIG. 2. (Color online) Cross-sectional TEM images. The white arrows indicate the location of the Fe/Sm-Co interface. A bright field (a) and a dark field (b) image of the $T100$ sample. A bright field (c) and a dark field (d) image of the $T400$ sample. The contrast in the dark field images is due to the alignment of the grains. (e) TEM diffraction pattern for the $T400$ sample. The absence of separate Fe diffraction spots indicates that the Fe spots most likely overlap with the identified Cr spots, suggesting a good alignment between the Fe and the Cr buffer layers.

4(b)]. For the $T400$ sample, the Co curve looks similar to the Fe curve while, for the $T100$ sample, the Co curve resembles the Sm curve.

To account for the low-angle attenuation effect in the measured XRMS magnetization curves, we calculated the electric field intensity profiles inside the film layers. For each sample, the electric field intensity profiles were calculated based on a model film structure that was approximated by one set of Sm, Co, and Fe concentration profiles. From the EDS results, the $T400$ film has a more intermixed interface. It was assumed that the major difference between the $T100$ and $T400$ films exists only in the region between the near-interface Sm-Co sublayers and the Fe sublayers. Intermixing was approximated using error functions with a parameter σ that controls the width of the intermixed region. For each sample, three different profiles were calculated to represent
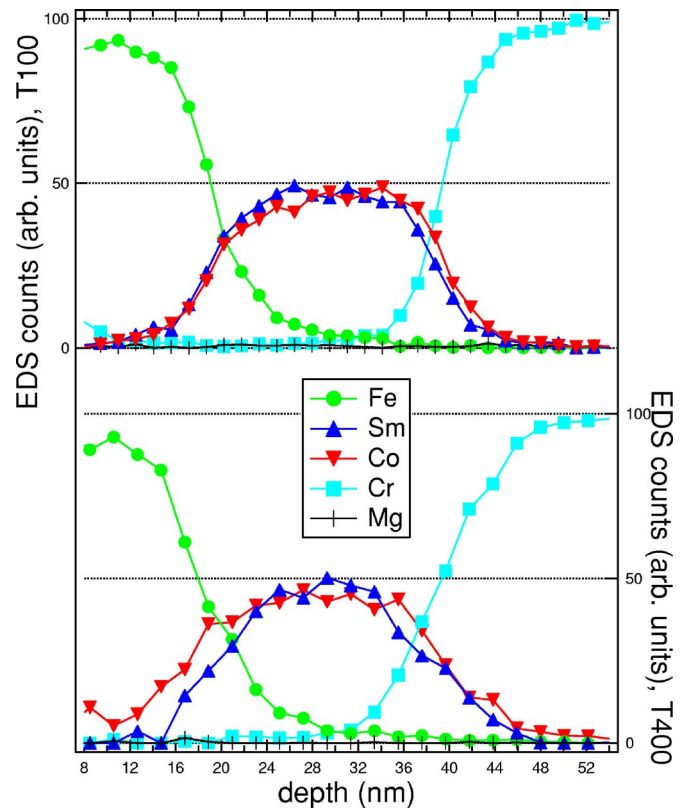

FIG. 3. (Color online) Cross-sectional EDS line scan profiles from the $T100$ and $T400$ samples.

the resonant energies of Fe L_3, Co L_3, and Sm M_4 from which the three element-specific magnetization curves were obtained as shown in Figs. 5 and 6. The calculated electric field intensity profiles show that absorption was significant in each resonant layer, suggesting the layers at different depths contribute differently. Thus our XRMS magnetometry measurements can provide not only element-sensitive but also depth-sensitive magnetization information.

Based the same model film structure, simulated magnetization curves were obtained from micromagnetic calculations. The simulated curves were compared with the SQUID magnetometry results to reproduce the experimental results. For this comparison, simulated demagnetization curves of 1-nm-thick sublayers were weighted equally because the SQUID measures the volume-averaged magnetic response. In contrast to the SQUID, XRMS is depth sensitive. Thus, the simulated demagnetization curves of 1-nm-thick sublayers were extracted from the $T100$ and $T400$ simulations and weighted using the calculated electric field intensity profiles and the assumed model concentration profiles. Then, the weighted curves were summed to give the simulated element-specific magnetization curves $M(H)$ as

$$M(H)_{\text{Sm, Co, or Fe}} = \sum_{L=1}^{40} [I(z_L)c(z_L)m(z_L,H)Ms(z_L)], \quad (1)$$

where L is the sublayer number, z_L is the depth from the surface for the sublayer L, I is the local e-field intensity, c is the resonant element concentration (Sm, Co, or Fe), m is the
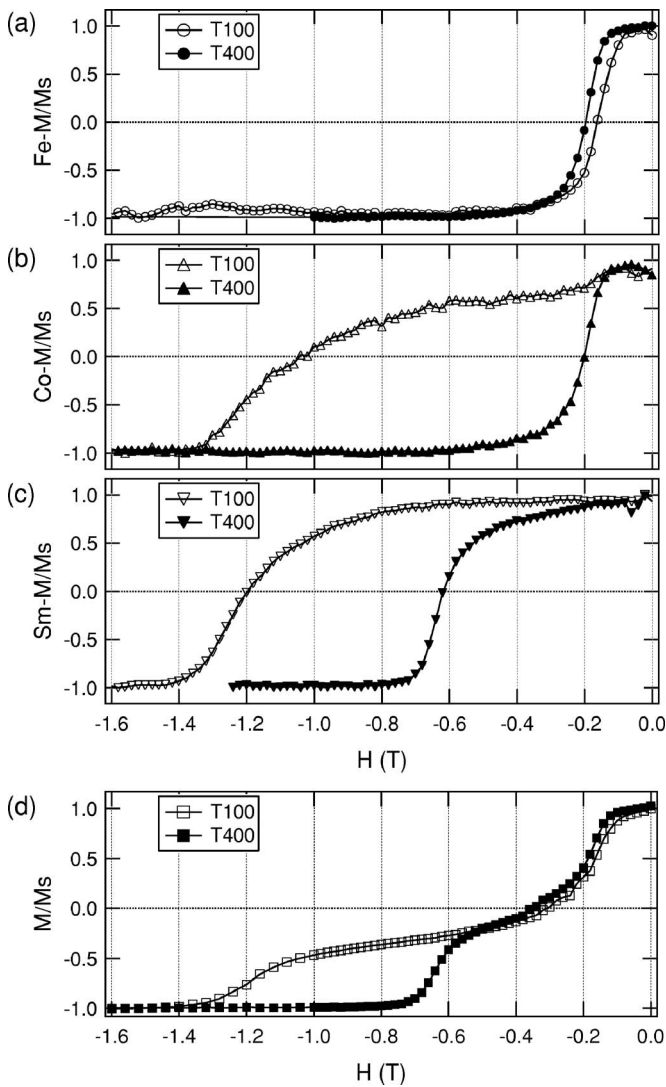
FIG. 4. Element-specific magnetization curves for the *T*100 and *T*400 samples measured at 200 K using XRMS. (a) Fe, (b) Co, and (c) Sm magnetization. (d) SQUID magnetization curves at 200 K.

FIG. 5. (Color online) (a)–(c) Calculated electric field intensity profiles for the *T*100 sample at the Fe L_3, Co L_3, and Sm M_4 resonant energies. (d) Concentration profiles used in the calculations. The concentration change across the Sm-Co/Fe interface is modeled by an error function initially and then refined to better match the micromagnetic result to the SQUID and XRMS results.

magnetization direction $(-1 < m < +1)$, and M_s is the local saturation magnetization. The process of setting model concentration profiles and calculating electric field and micromagnetic curves was done iteratively. After comparing the XRMS curves with the weighted simulation curves, the assumed model concentration profiles were refined to better match the simulated curves with the experimental curves. The adjustable parameters were the interface width σ and relative Co compositions in the Fe layer. In order to account for the effect of the diffused Co atoms present in the Fe layer, the magnetic parameters M_s and A of the Fe layer were adjusted according to the relative concentration of the diffused Co. The SQUID magnetometry curves were best reproduced with $\sigma = 1$ and 3 nm for the *T*100 and *T*400 samples, respectively, as shown in Figs. 7(a) and 7(d). The simulated demagnetization curves of 1-nm-thick sublayers at various depths were plotted for the *T*100 and *T*400 samples in Figs. 7(b) and 7(e). These simulated curves were based on the model concentration profiles in Figs. 5(d) and 6(d). The
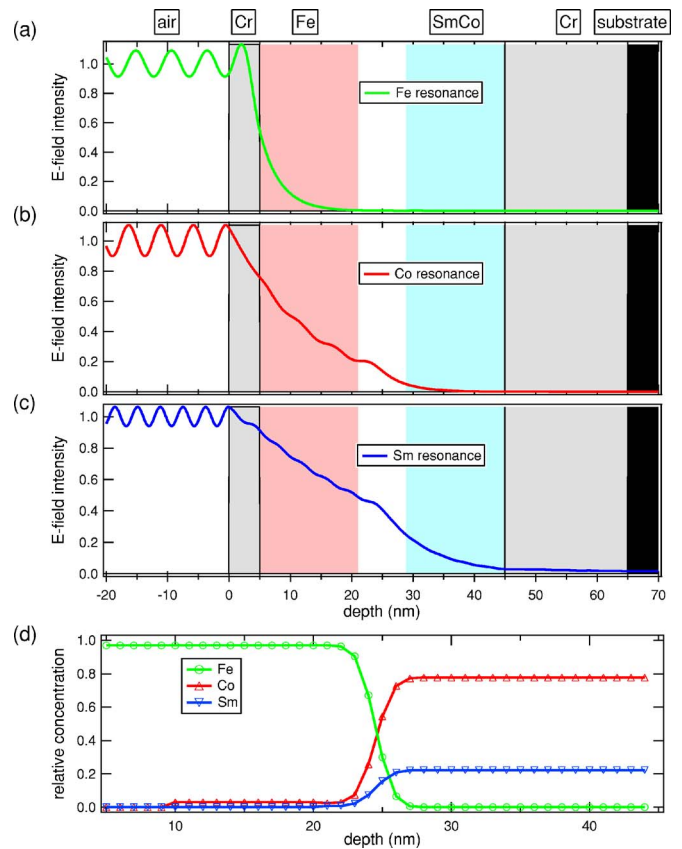
XRMS experimental and the weighted simulation curves are compared in Figs. 7(c) and 7(f) for each sample. The discrepancy between the experimental and simulated results near the irreversible switching fields of the Sm-Co layer stems from the limitation of the assumed coherent rotation in the micromagnetic simulations. Away from the irreversible switching fields, the measured and simulated element-resolved magnetization curves are in good agreement, justifying the concentration models that the simulations are based upon.

For each sample, when comparing the magnetization curve from the SQUID and the simulated magnetization curve, the simulation results were very sensitive to modifications at the Sm-Co/Fe interface. However, the simulation results were not very sensitive to small details of the Fe layer. For example, a few percent of the diffused Co atoms in the Fe layer changes the net simulated curve of the *T*100 sample negligibly. This stems from the fact that the difference between Fe and Co magnetic parameters is not as drastic as the difference between Fe and Sm-Co parameters. On the contrary, when comparing the XRMS and weighted simulation results, even a small change in the concentration profile in the Fe layer can have a significant effect on the agreement between the two results. This demonstrates the effectiveness of our combined approach of XRMS, micro-
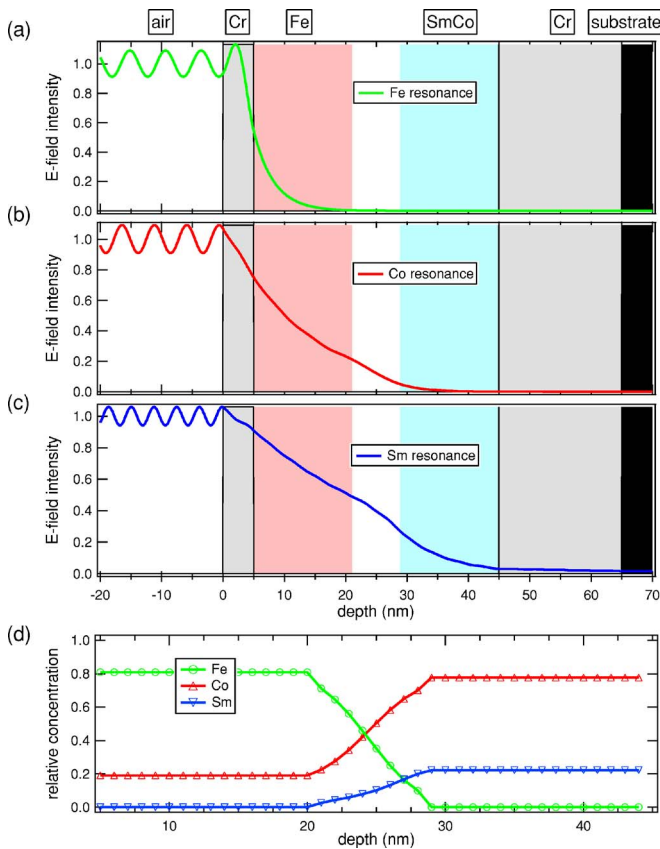
FIG. 6. (Color online) (a)–(c) Calculated electric field intensity profiles for the $T400$ sample at the Fe L_3, Co L_3, and Sm M_4 resonant energies. (d) Concentration profiles used in the calculations. The concentration change across the Sm-Co/Fe interface is modeled by an error function initially and then refined to better match the micromagnetic result to the SQUID and XRMS results.
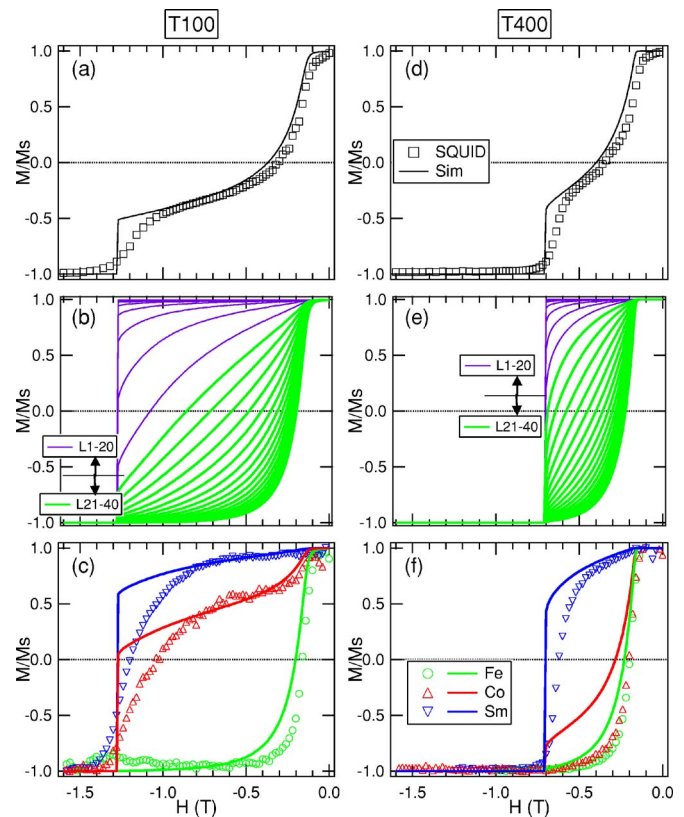

FIG. 7. (Color online) (a),(d) Comparison between micromagnetic calculations and SQUID demagnetization curves for the $T100$ and $T400$ samples. (b),(e) Simulated demagnetization curves for each 1-nm-thick sublayer. The layers $L1$–$L20$ represent Sm-Co sublayers, and the layers $L21$–$L40$ represent Fe sublayers. (c),(f) Weighted simulation and XRMS experimental curves.

magnetic, and depth-sensitivity calculations, in comparison with only bulk magnetometry and micromagnetic calculation.

For the $T100$ sample, the x-ray penetration depth for the Co XRMS magnetization curve measurement is less than that for Sm. This difference contributes to the observed difference between the Sm and Co XRMS curves. However, the penetration depth difference alone could not reproduce the kink at $H=-0.1$ T in the Co XRMS curve [Fig. 7(c)]. The kink occurs at the field where the Fe curve starts to decay, and the presence of the kink in the Co curve suggests that some of the Co atoms near the interface follow the field dependence of the Fe. This effect was approximated by adding 3% Co concentration in the Fe layer up to 15 nm away from the Sm-Co/Fe interface, as shown in Fig. 5(d). The added Co concentration approximates diffused Co atoms into the Fe layer, and, because the concentration is small, the electric field profiles were not modified noticeably. However, the combined profile of the electric field intensity and concentration was changed, since the contribution to the collected dichroic signal is higher due to higher electric field intensities at smaller depths.

The same approach was implemented to reproduce the XRMS results from the $T400$ sample with weighted simu-

lated curves. In contrast to the $T100$ sample case, the Co XRMS curve is almost the same as the Fe XRMS curve for the $T400$ sample. The x-ray penetration depth at the Co resonant energy is expected to be different between the two samples since the interfacial intermixing and the Co diffusion result in modified relative compositions and thus absorption at various depths. However, as seen in the calculated electric field profiles, this penetration depth effect alone is not drastic enough to cause the difference between the Co XRMS curves. The Co XRMS magnetization curve matches the weighted simulated curve when a significant amount of Co diffusion was introduced in the concentration profiles, as shown in Fig. 6(d). This model is consistent with the EDS result that shows higher Co diffusion into the Fe layer for $T400$ (Fig. 3) in addition to the Sm-Co/Fe intermixing.

In comparison with the $T100$ sample, the $T400$ sample has a wider intermixed region at the Sm-Co/Fe interface with additional Co diffusion into the Fe layer. In the current discussion, two types of Co diffusion are distinguished arbitrarily and treated separately. The first type of the Co diffusion is accompanied by Sm and Fe diffusion due to intermixing at the interface, which was approximated by the error function in the concentration profile models. The second type is the additional Co diffusion into the Fe layer, which was approximated by adding a fraction of Co in the Fe

layer. The additional Co diffusion in the Fe layer of the T400 sample, as observed in the EDS scans, is consistent with an earlier study on thermal processing with similarly made Sm-Co/Fe films[7] where Co diffusion into the Fe layer was observed by electron energy loss spectra (EELS) from an annealed Sm-Co/Fe film. Similarly, in $Sm(Co,Cu)_5$/Fe multilayer films, EELS maps also revealed that Co diffusion across interfaces was more significant in comparison with Sm diffusion.[6]

From the T400 sample, the Co magnetization curve is dominated by the signals from the additionally diffused Co atoms in the Fe layer due to higher electric field intensities in their new depth positions. This second type of diffusion of Co atoms in the T400 sample may act as an intermediate connection providing an enhanced coupling effectiveness across the Fe and Sm-Co layers. In calculating the weighed simulation curves in Fig. 7(f), it was assumed that the diffused Co mimics the magnetization behavior of the surrounding Fe atoms. This assumption was justified by the fact that the nucleation fields are almost the same for the Co and Fe XRMS curves. This suggests a strong coupling between the diffused Co atoms and surrounding Fe atoms in the Fe layer. Meanwhile, the Co moments in the Sm-Co layers are already well coupled with the Sm moments in the Sm-Co crystalline structure. The good agreement between the experimental and calculated Co curves in Fig. 7(f) indicates that the change in Co magnetization process across the interface is gradual, as in Fig. 7(e). This interpretation is consistent with the cross-sectional TEM results shown in Fig. 2 where the T400 sample shows better grain alignment.

V. SUMMARY AND CONCLUSION

A comparative study on two films with different interface characteristics, induced by changing the growth temperature of Fe, was reported. An enhanced exchange coupling effectiveness between the Sm-Co and Fe layers is confirmed in the Sm-Co/Fe bilayer prepared at a higher temperature where the interdiffusion of Co across the interface becomes prominent. With a unique combined approach of depth- and element-sensitive XRMS magnetometry measurements and micromagnetic simulation with depth-sensitive profiles, we found evidence of the presence of the diffused Co in the Fe layer and extracted the magnetization behavior of the diffused Co. The diffused Co atoms show the same magnetization behavior as the surrounding Fe atoms and contribute to the observed enhancement of the exchange coupling effectiveness between the Fe and Sm-Co layers. The models used in the concentration profiles to account for the additional Co diffusion are simple, and the approach assumes lateral homogeneity. However, despite the simplicity, the experimental element-resolved magnetization curves were reproduced well with the calculated results, unambiguously singling out the magnetization behavior of the diffused Co atoms and their contribution to the improved exchange coupling effectiveness.

[1] E. F. Kneller and R. Hawig, IEEE Trans. Magn. **27**, 3588 (1991).

[2] R. Skomski and J. M. D. Coey, Phys. Rev. B **48**, 15812 (1993).

[3] E. E. Fullerton, J. S. Jiang, and S. D. Bader, J. Magn. Magn. Mater. **200**, 392 (1999).

[4] J. Kim, K. Barmak, M. De Graef, L. H. Lewis, and D. C. Crew, J. Appl. Phys. **87**, 6140 (2000).

[5] D. C. Crew, J. Kim, L. H. Lewis, and K. Barmak, J. Magn. Magn. Mater. **233**, 257 (2001).

[6] J. Zhang, K. Takahashi, R. Gopalan, and K. Hono, Appl. Phys. Lett. **86**, 122509 (2005).

[7] J. S. Jiang, J. E. Pearson, Z. Y. Liu, B. Kabius, S. Trasobares, D. J. Miller, S. D. Bader, D. R. Lee, D. Haskel, G. Srajer, and J. P. Liu, Appl. Phys. Lett. **85**, 5293 (2004).

[8] C. Kao, J. B. Hastings, E. D. Johnson, D. P. Siddons, and G. C. Smith, and G. A. Prinz, Phys. Rev. Lett. **65**, 373 (1990).

[9] J. W. Freeland, K. Bussmann, P. Lubitz, Y. U. Idzerda, and C.-C. Kao, Appl. Phys. Lett. **73**, 2206 (1998).

[10] J. W. Freeland, J. C. Lang, G. Srajer, R. Winarski, D. Shu, and D. M. Mills, Rev. Sci. Instrum. **73**, 1408 (2001).

[11] This incident angle 10° is relatively low considering that the critical angle θ_C of total external reflection of each constituent element is typically a few degrees at the x-ray energies used here. For example, θ_C is $\approx 3.4°$ for the Cr capping layer at the Fe L_3 absorption edge.

[12] L. G. Parratt, Phys. Rev. **95**, 359 (1954).

[13] D. K. G. de Boer, Phys. Rev. B **44**, 498 (1991).

[14] D. T. Cromer and D. Liberman, J. Chem. Phys. **53**, 1891 (1970).

[15] J. O. Cross, M. Newville, J. J. Rehr, L. B. Sorensen, C. E. Bouldin, G. Watson, T. Gouder, G. H. Lander, and M. I. Bell, Phys. Rev. B **58**, 11215 (1998).

[16] B. L. Henke, E. M. Gullikson, and J. C. Davis, At. Data Nucl. Data Tables **54**, 181 (1993).

[17] http://llgmicro.home.mindspring.com

[18] A. E. Ray and K. J. Strnat, IEEE Trans. Magn. **MAG-8**, 516 (1972).

[19] R. S. Perkins, S. Gaiffi, and A. Menth, IEEE Trans. Magn. **MAG-11**, 1431 (1975).

[20] K. S. V. L. Narasimhan and W. E. Wallace, IEEE Trans. Magn. **MAG-13**, 1333 (1977).